






Communication

Broadband Polarization Rotator and Splitter Based on 70 nm-Etched Waveguides on SOI Platform

Ye Tian ¹, Zhe Kang ^{2,*}, Tingge Dai ³, Peipeng Xu ¹, Yan Li ¹, Yegang Lv ¹ and Xiaowei Zhang ^{1,*}¹ Department of Electrical Engineering and Computer Science, Ningbo University, Ningbo 315211, China² Centre for Optical and Electromagnetic Research, College of Optical Science and Engineering, National Engineering Research Center for Optical Instruments, Ningbo Innovation Center, Zhejiang University, Hangzhou 310058, China³ Department of Information Science and Electronics Engineering and Cyrus Tang Center for Sensor Materials and Applications, Zhejiang University, Hangzhou 310027, China

* Correspondence: zhe_kang@zju.edu.cn (Z.K.); zhangxiaowei@nbu.edu.cn (X.Z.)

Abstract: The standard silicon photonic platforms provide three-step silicon etching, i.e., 220 nm for full etching, 70 nm for shallow etching, and 130 nm (or 150 nm) for slab etching. Previously reported mode-evolution-based polarization rotators and splitters (PSRs) usually employ 130 nm-etched slab waveguides for adiabatic TM_0 -to- TE_1 conversion, however, they are not compatible with the platforms adopting 150 nm-etching techniques. In this paper, we demonstrate a broadband PSR based on 70 nm-etched slab waveguides, which is compatible with all the platforms. The PSR consists of a bi-level taper and an inverse-tapered coupler. The length of the polarization rotator shrinks from hundreds to only thirty microns by employing the 70 nm-etched slab waveguides, while a high efficiency of >95% is achieved, covering an ultra-wide bandwidth from 1250 nm to 1650 nm. The proposed PSR shows superior performance over S, C, and L bands. Low cross-talk of <−20 dB and a loss of <1.5 dB are experimentally confirmed over a wavelength range of 75 nm.

Keywords: polarization delivery; silicon photonics; silicon passive devices

Citation: Tian, Y.; Kang, Z.; Dai, T.; Xu, P.; Li, Y.; Lv, Y.; Zhang, X.

Broadband Polarization Rotator and Splitter Based on 70 nm-Etched Waveguides on SOI Platform.

Photonics **2022**, *9*, 758. <https://doi.org/10.3390/photonics9100758>

Received: 22 September 2022

Accepted: 4 October 2022

Published: 12 October 2022

Publisher's Note: MDPI stays neutral with regard to jurisdictional claims in published maps and institutional affiliations.



Copyright: © 2022 by the authors. Licensee MDPI, Basel, Switzerland. This article is an open access article distributed under the terms and conditions of the Creative Commons Attribution (CC BY) license (<https://creativecommons.org/licenses/by/4.0/>).

1. Introduction

Silicon photonic is one of the most attractive techniques for realizing high-density optoelectronic integrated circuits on a single chip because of its potential advantages, such as low power consumption and compatibility with the advanced manufacturing process of microprocessors, known as the complementary metal-oxide-semiconductor (CMOS) process [1,2]. This technology is based on high-index-contrast materials, allowing for tight optical confinement on the nanometer scale. On the other side, this property also leads to strong birefringence and polarization dependence in the waveguides. To solve this problem, polarization diversity devices, including polarization beam splitters (PBSs) [3–10], polarization rotators (PRs) [11–14], and polarization splitter–rotators (PSRs), are widely equipped on the integrated circuits, acting as the fundamental building blocks in many applications, such as polarization multiplexing [15] and coherent optical communication [16]. Among them, PSRs are often preferred because they convert both orthogonal polarizations to fundamental transverse electric (TE_0) polarization, so that the rest of the functional devices can work in the same polarization.

Recently, various PSRs have been reported based on either the hybrid mode coupling or mode evolution mechanism. To separate and rotate the fundamental transverse magnetic (TM_0) mode, the former ones usually convert TM_0 mode to a hybrid mode (partial TE and partial TM) using asymmetric waveguide structures and then convert it to TE_0 mode [17–19]. These kinds of devices are highly efficient at operation wavelength and relatively compact in footprint. However, they are intrinsically wavelength dependent and fabrication sensitive due to the coupling mechanism. The latter ones consist of an adiabatic

polarization rotator (APR) and a mode de-multiplexer (MD). Firstly, the APR converts TM_0 mode into the first-order quasi-TE (TE_1) mode, typically using a bi-level adiabatic taper [20]. Afterwards, the TE_1 mode can be separated and converted to TE_0 mode using MD structures such as adiabatic couplers [21–24] or Y-branches [25]. Benefiting from the adiabatic mechanism, the bandwidth and fabrication tolerance of devices can be effectively improved. However, the length of devices is also expansively increased (hundreds of microns) to complete the mode evolution process. Efforts have been made to shrink the size of MDs by employing structures such as multimode interference couplers [26,27] and asymmetrical directional couplers [28], but the optimization of the footprint of APRs is still challenging. In [29], the APR is shortened by optimizing the bi-level taper using the particle swarm optimization (PSO) method, but the adiabatic character is no longer kept so that multiple devices are designed for different working bands.

Generally, commercial multiproject wafer (MPW) services provide standard etching depths, including 220 nm for full etching and 70 nm for shallow etching. As to the slab waveguides, the foundries offer different etching depths, i.e., 130 nm (AMF, Singapore) and 150 nm (IMEC, Ghent, Belgium; HOPHO, Chengdu, China, etc.) [30]. Previously reported PSRs adopt the APR based on bi-level tapers with 130 nm-etched slab waveguides, the length of which is typically above 100 μm [20,23]. However, these kinds of PSRs are not compatible with all the MPW services. In comparison, here, we demonstrate an APR-based PSR that is compatible with all the MPW services, offering etching depths of 220 nm and 70 nm. A novel APR based on bi-level taper with 70 nm-etched slab waveguides is proposed, and a high efficiency of >95% for TM_0 -to- TE_1 conversion is achieved over 1250 nm to 1650 nm with only 30 μm device length. By connecting the APR to a mode de-multiplexer, we predict this PSR has a low loss of <1 dB and low cross-talk of below –20 dB over S, C, and L bands. This PSR is fabricated through the commercial MPW program, and the measurement results show a cross-talk of <–20 dB and loss of <1.5 dB within the bandwidth of 1500–1575 nm, which well matches the prediction.

2. Device Design

The schematic diagram of the proposed PSR is shown in Figure 1a, in which the dark blue regions indicate the rib waveguide that has a height of $H = 220$ nm, and the light blue regions indicate the partially etched slab waveguides with a height of $H_s = 150$ nm. The strip waveguide with a width of 0.5 μm (W_{in}) is used for the injection of TE_0 and TM_0 modes. This PSR consists of two parts: a bi-level taper performing the APR and an inverse-tapered coupler as the MD. Between them, a tapered structure with a length of L_t is inserted for components connection and size transition. The whole device is covered by a SiO_2 upper cladding. When TE_0 mode is injected, it propagates through the device without any conversion and outputs from the through port. When TM_0 mode is injected, it will first be converted to the TE_1 mode by the APR and then coupled to the TE_0 mode in the cross-port. The electric intensity profiles in the cross-section along the propagation direction are illustrated in the insets. Specifically, the height of the MD is designed as 150 nm to match the output of PR. Since the propagation of TM_0 polarization within the waveguides of 150 nm in height would be lossy due to the mode leakage, the MD can further filter the residual TM_0 mode to enhance performance. At the output of PSR, the height of through/cross-ports are gradually increased to 220 nm using the negative tapers. Both output ports will finally access the single-mode waveguide for high-order mode elimination and device interconnection. The detailed parameters and corresponding values are listed in Table 1.

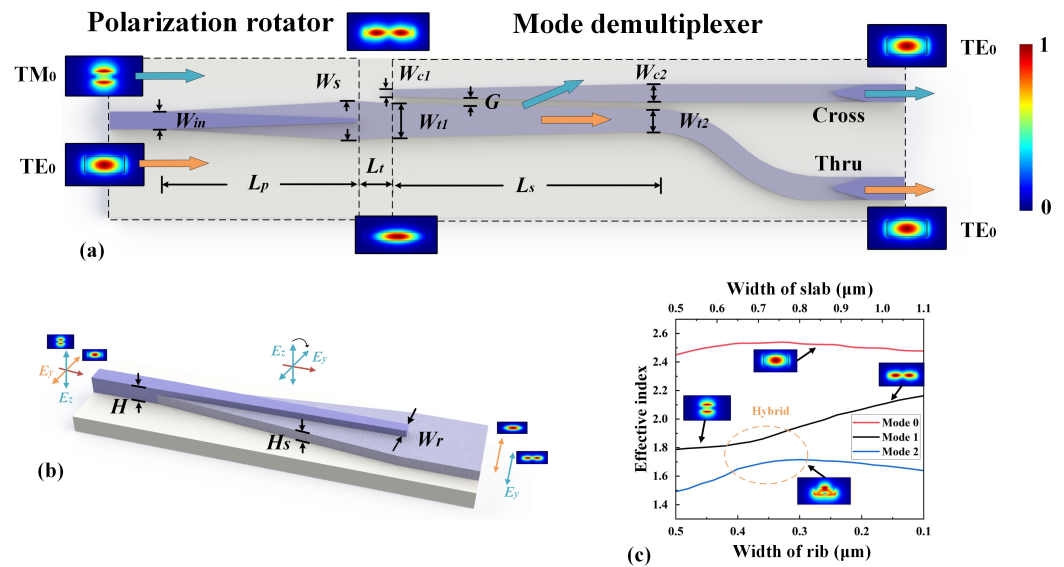


Figure 1. (a) The schematic diagram of the proposed PSR. (b) The 3D schematic diagram of the APR. (c) The calculated effective refractive indices of the first three modes as a function of the width variation for both slab and rib waveguides.

Table 1. Parameters and values of the PSR.

Parameters	Values (μm)	Parameters	Values (μm)
W_{in}	0.5	W_{t1}	0.95
W_r	0.1	W_{t2}	0.65
W_s	1.1	W_{c1}	0.2
L_t	5	W_{c2}	0.5
L_s	100	H	0.22
G	0.2	H_s	0.15

A bi-level taper with an asymmetrical cross-section is specially designed to realize adiabatic polarization rotation from TM_0 mode to TE_1 mode, as shown in Figure 1b. The length of the APR is labeled as L_p . The width of the slab is symmetrically increased from W_{in} (fixed at 500 nm for easy connection with single-mode waveguide) to W_s , and the width of the rib decreases from W_{in} to W_r . Taking the fabrication precision into consideration, W_r is set as 100 nm. W_s is set as 1.1 μm for the broadband phase matching between TM_0 and TE_1 mode. The effective refractive indices of the first three modes (TE_0 , TM_0 , and TE_1) at 1550 nm are calculated as a function of the width variation for both slab and rib waveguides, which is depicted in Figure 1c. The Mode 0 and Mode 1 are originally set as TE_0 and TM_0 mode, respectively. When TE_0 mode is injected to the APR, the index variation along the propagation is depicted by the red line. This mode will propagate through the bi-level taper without conversion because its index maintains a high-level, and no mode hybridization appears during the propagation. In the case of TM_0 injection, the index variation is depicted by the black line. The mode hybridization occurs at the widths of around 0.36 μm /0.71 μm for the rib/slab waveguides, the electric intensity field of the hybrid mode is shown in the inset. As the width of rib/slab further decreases/increases, the hybrid mode will finally be converted to the TE_1 mode according to the mode evolution theory [31].

The length of APR (L_p) is swept from 20 μm to 70 μm to investigate the conversion efficiency over an ultra-wide band from 1250 nm to 1650 nm. The simulation is carried out by using the 3D finite-difference time-domain method (3D FDTD). Figure 2a shows the results in a form of 3D surface graph. We can see that an efficiency of above 90% is achieved over the whole band when L_p reaches 20 μm . As the length exceeds 30 μm , the efficiency for this band achieves 95% or above, indicating a highly efficient conversion from TM_0 mode to TE_1 mode with a compact footprint. Figure 2b shows the optical power

distribution when TM_0 mode is injected to the APR (L_p is set as $30\ \mu\text{m}$), in which the polarization evolution along the propagation axis is also shown. Three wavelengths of 1250 nm, 1450 nm, and 1650 nm are selected to examine the performance of the APR. We can see clearly the rotation from input E_z components (TM-polarized) to the E_y components (TE-polarized), while the input TM_0 modes are effectively converted to TE_1 modes at all the wavelengths. We can also observe that the location of mode evolution trends to right shift for long wavelengths because the phase-matching point moves along the propagation direction as the wavelength increases.

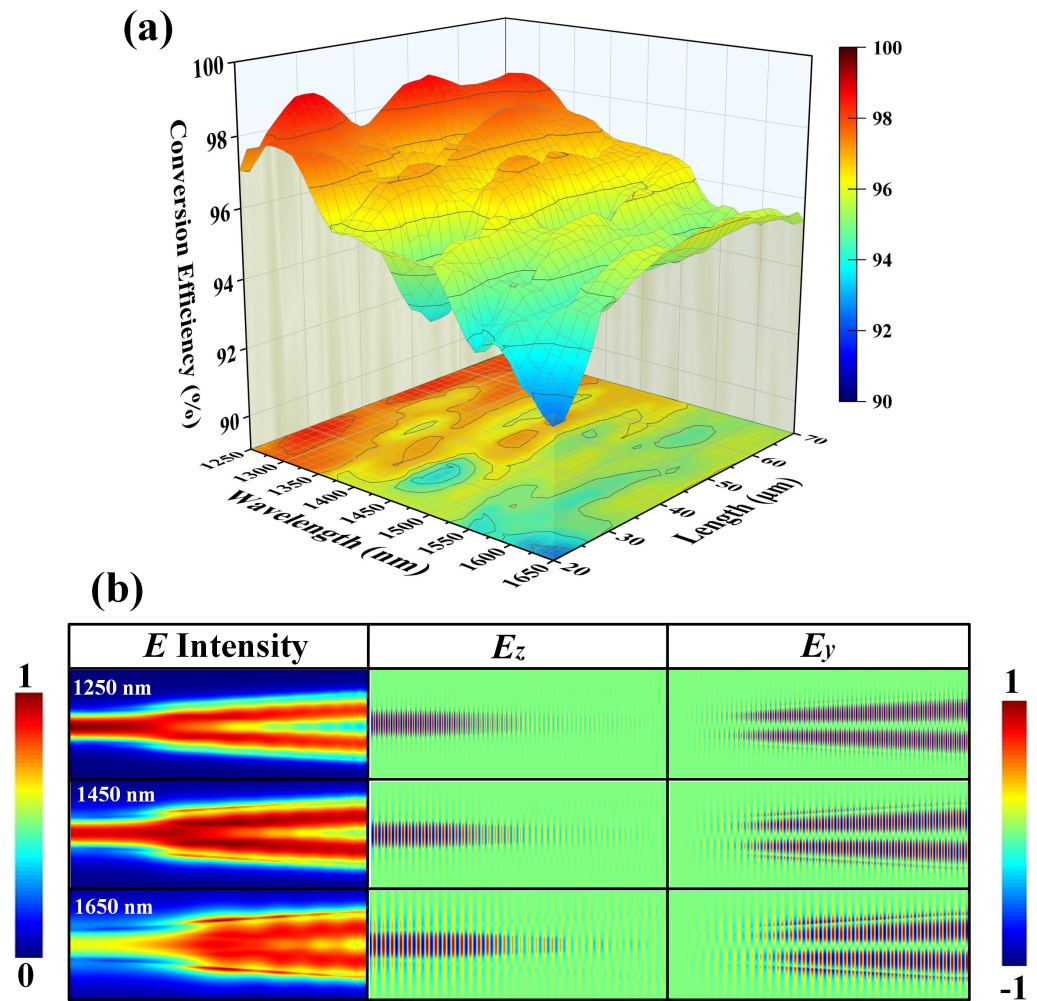


Figure 2. (a) Calculated conversion efficiency over a bandwidth of 1250–1650 nm for different lengths from 20 μm to 70 μm . (b) Optical power distribution and the modal field evolution along the propagation axis of the APR at the wavelengths of 1250 nm, 1450 nm, and 1650 nm.

As illustrated in Figure 1a, an inverse-tapered coupler is employed as the MD which routes the TE_0 and TE_1 modes to desired output ports. The TE_0 mode would propagate through the MD without conversion and output from the through port, while the TE_1 mode would couple to TE_0 mode and output from the cross-port. The design principle of MD is similar to [20] but is applied to the waveguides with a height of 150 nm. The width of the through waveguide decreases from $0.95\ \mu\text{m}$ to $0.65\ \mu\text{m}$, whereas the width of the cross-waveguide increases from $0.2\ \mu\text{m}$ to $0.5\ \mu\text{m}$. The length of the taper is set as 100 μm for the adiabatic mode evolution, and the gap between the tapers is fixed as $0.2\ \mu\text{m}$. By connecting the APR with MD, the simulated optical power distribution in the designed PSR is shown in Figure 3a. At the wavelength of 1550 nm, the injected TE_0 mode outputs

from the through port directly. Meanwhile, the TM_0 mode is converted to TE_0 mode and outputs from the cross-port. When TE_0 or TM_0 mode is injected, the transmissions of both TE_0 and TM_0 modes from the through/cross-ports are monitored and shown in Figure 3b,c, respectively. At a wavelength range of 1450 nm to 1650 nm, the insertion losses (ILs) of the desired mode are less than 1 dB for both polarizations, and the cross-talk induced by the unwanted modes are lower than -20 dB. The proposed PSR exhibits a superior performance with a broad operating wavelength covering S, C, and L bands.

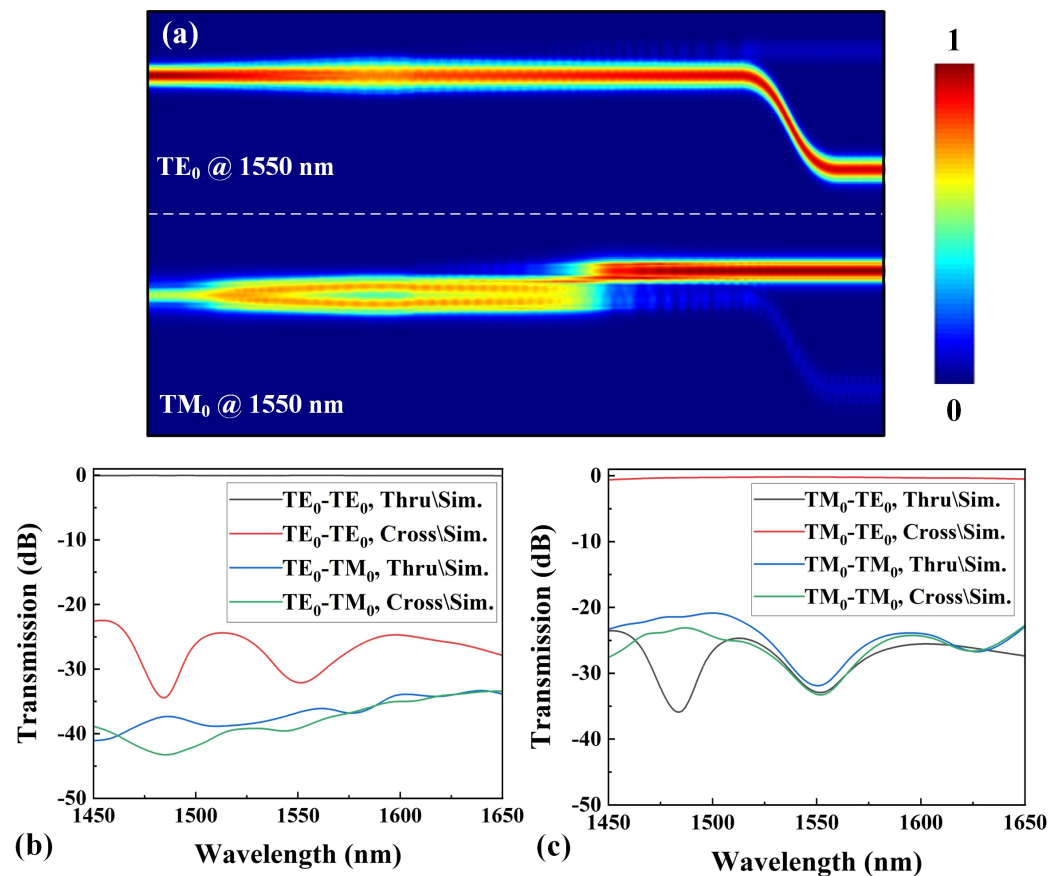


Figure 3. (a) Simulated optical power distribution along the designed PSR in case of TE_0 or TM_0 injection. Transmission spectrum for (b) TE_0 injection and (c) TM_0 injection.

3. Fabrication and Measurement

The proposed device was fabricated through a commercial MPW run (HOPHO Inc., Xingu Industrial Park, Shuangliu District, Chengdu City, China). It was processed on an SOI wafer with a 220 nm top silicon layer and a 2 μm buried oxide layer. To define the pattern of the devices, 193 nm-deep ultraviolet (UV) photolithography was used, while inductively coupled plasma (ICP) was used to etch the silicon layers. Finally, a silica upper-cladding was deposited on the structure by a plasma-enhanced chemical vapor deposition (PECVD) process. Grating couplers (GCs) are implemented for light coupling from fibers; the periods of grating couplers for the TE and TM modes are 620 nm and 984 nm, respectively. The fill factor and etching depth of the grating couplers are 0.5 and 70 nm, respectively. Figure 4a shows the optical micrograph of the fabricated PSR; the rectangles covering the PSRs are the trenches that have no influence on the device. To fully characterize the performance, four test structures with the same geometry but different GCs are fabricated. A tunable laser (Santec TSL-550) is used as the source and an optical power meter is used to measure the optical power.

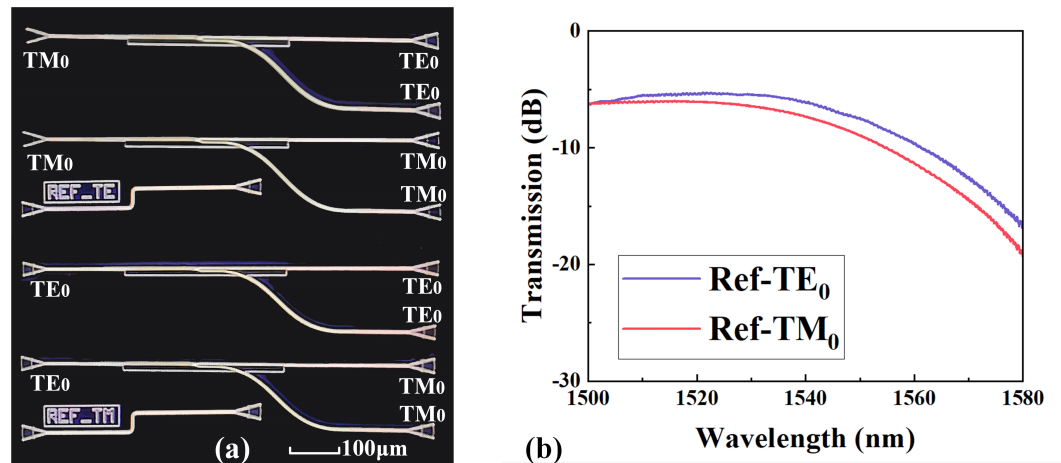


Figure 4. (a) Optical micrograph of the fabricated devices. (b) Transmission responses of the reference grating couplers.

The transmission spectra of the reference grating couplers are shown in Figure 4b. The maximum coupling efficiencies of TE₀ and TM₀ grating are 5 dB/facet and 6 dB/facet, accompanied with an attenuation of around 12 dB at the long wavelengths. Limited by the tunable range of lasers and the bandwidth of GCs, the measurement is carried out within a bandwidth from 1500 nm to 1575 nm. The experimental results are shown in Figure 5 (solid curves). As a comparison, the simulation results are also attached in Figure 5 (dashed curves). We see that for TE₀ injection, the IL is less than 1 dB, and the cross-talk is below −20 dB for the whole band. For TM₀ injection, the IL increases as the wavelength rises up because the sidewall roughness of the MD induces extra propagation loss for the TE₁ mode. However, the IL for TM₀ injection is still less than 1.5 dB, while the cross-talk is kept below −20 dB over the band. However, the transmissions of the TE-TE Cross, TE-TM Thru, TE-TM Cross, TM-TE Thru, and TM-TM Thru ports are far lower than the simulation results at the long wavelength. Since the grating coupler introduces a huge power attenuation at the long wavelength, the cross-talk cannot be detected due to the limited sensitivity of the power meter. Similarly, the transmission of the TM-TM Cross-port is also out of detection for the whole band.

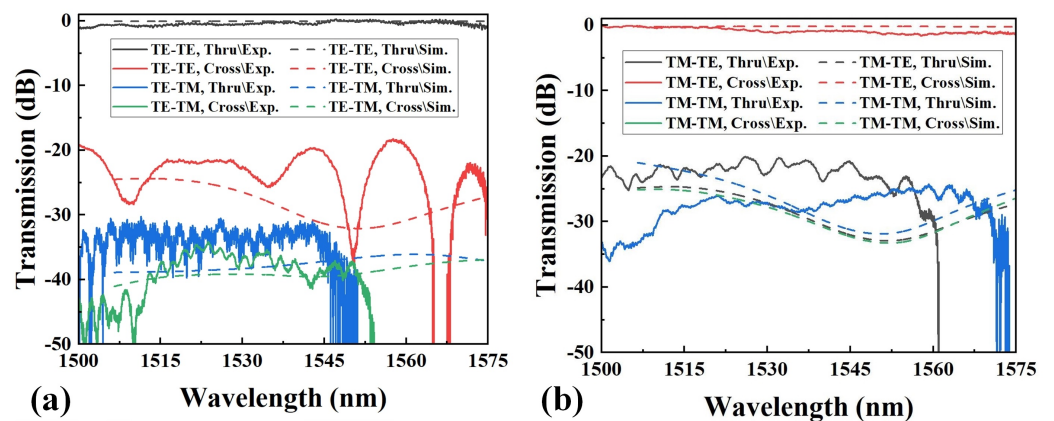


Figure 5. Measured transmission spectra for the (a) TE₀ and (b) TM₀ injection.

Table 2 shows a comparison among reported APR-based PSRs on the SOI platform. We can find that the APR of our design has an apparently compact size. Additionally, the proposed PSR exhibits a nice performance over a broad bandwidth. We note that the measured results are limited by our experimental setup. A broader operation bandwidth would probably be obtained if either the laser source is updated or the GCs are further optimized. We will make efforts to fix these problems in our future work.

Table 2. Performance comparison of APR-based PSRs on the SOI platform.

Reference	APR Length (μm)	IL (dB)	Cross-Talk (dB)	Bandwidth (nm)	Etching Depth (nm)	Exp./Sim.
[20]	100	1.6	−13	50	220/130	Experiment
[21]	53.5	0.2	−15	320	220/130	Simulation
[22]	53.5	0.73	−12.1	110	220/130	Experiment
[25]	70	1	−14	100	220/130	Experiment
[27]	100	0.6	−17.6	110	220/70	Experiment
This work	30	1	−20	200	220/70	Simulation
This work	30	1.5	−20	75	220/70	Experiment

4. Conclusions

We experimentally demonstrated a broadband PSR based on a bi-level taper and an inverse-tapered coupler. The device is designed with a 150 nm-high slab waveguide that suits the active silicon photonics platform. The footprint of the APR is significantly shrunk from hundreds to tens of microns while maintaining a high conversion efficiency of >95% over 1250 nm to 1650 nm. Connecting the APR with the mode splitter, the device exhibits a low loss of <1 dB and a cross-talk of <−20 dB over a broadband from 1450 nm to 1650 nm. The proposed PSR is fabricated through the commercial MPW program, and the loss of <1.5 dB and cross-talk of <−20 dB are confirmed for a bandwidth of 75 nm. This device offers a promising solution for ultra-compact PSRs and potential applications in integratable optical communication links and optical interconnection networks.

Author Contributions: Conceptualization, Y.T. and Z.K.; methodology, Y.T. and Y.L. (Yan Li); software, Y.L. (Yegang Lv); investigation, Y.T.; data curation, Y.T., T.D. and P.X.; writing—original draft preparation, Y.T.; writing—review and editing, Z.H. and X.Z.; supervision, Z.K.; project administration, X.Z.; funding acquisition, X.Z. All authors have read and agreed to the published version of the manuscript.

Funding: This work was supported by the National Nature Science Foundation of China (NSFC) (62105167, 62075188, 61974078); Natural Science Foundation of Zhejiang Province (LQ22F050008, LY21F050007, LY21F040002, LQ21F040001); Natural Science Foundation of Ningbo (2021J074, 2021J059); Key Research and Development Program of Jiangsu Province (BE2021082).

Institutional Review Board Statement: Not applicable.

Informed Consent Statement: Not applicable.

Data Availability Statement: The data presented in this study are available on request from the corresponding author. The data are not publicly available due to the data also forming part of an ongoing study.

Acknowledgments: The authors express their appreciation to the anonymous reviewers for their valuable suggestions.

Conflicts of Interest: The authors declare no conflict of interest.

References

- Baehr-Jones, T.; Pinguet, T.; Lo Guo-Qiang, P.; Danziger, S.; Prather, D.; Hochberg, M. Myths and rumours of silicon photonics. *Nat. Photonics* **2012**, *6*, 206–208. [[CrossRef](#)]
- Shi, W.; Tian, Y.; Gervais, A. Scaling capacity of fiber-optic transmission systems via silicon photonics. *Nanophotonics* **2020**, *9*, 4629–4663. [[CrossRef](#)]
- Tian, Y.; Qiu, J.; Liu, C.; Tian, S.; Huang, Z.; Wu, J. Compact polarization beam splitter with a high extinction ratio over S+ C+ L band. *Opt. Express* **2019**, *27*, 999–1009. [[CrossRef](#)] [[PubMed](#)]
- Mao, S.; Cheng, L.; Zhao, C.; Fu, H. Ultra-broadband and ultra-compact polarization beam splitter based on a tapered subwavelength-grating waveguide and slot waveguide. *Opt. Express* **2021**, *29*, 28066–28077. [[CrossRef](#)] [[PubMed](#)]
- Li, C.; Dai, D.; Bowers, J.E. Ultra-broadband and low-loss polarization beam splitter on silicon. In *Optical Fiber Communication Conference*; Optical Society of America: Washington, DC, USA, 2020; p. Th1A.4.
- Ao, X.; He, S. Polarization beam splitters based on a two-dimensional photonic crystal of negative refraction. *Opt. Lett.* **2005**, *30*, 2152–2154. [[CrossRef](#)] [[PubMed](#)]

7. Wu, F.; Chen, M.; Xiao, S. Wide-angle polarization selectivity based on anomalous defect mode in photonic crystal containing hyperbolic metamaterials. *Opt. Lett.* **2022**, *47*, 2153–2156. [[CrossRef](#)] [[PubMed](#)]
8. Shi, X.; Zhang, J.; Fan, W.; Lu, Y.; Peng, N.; Rottwitt, K.; Ou, H. Compact low-birefringence polarization beam splitter using vertical-dual-slot waveguides in silicon carbide integrated platforms. *Photonics Res.* **2022**, *10*, A8–A13. [[CrossRef](#)]
9. Zhang, J.; Shi, X.; Zhang, Z.; Guo, K.; Yang, J. Ultra-compact, efficient and high-polarization-extinction-ratio polarization beam splitters based on photonic anisotropic metamaterials. *Opt. Express* **2022**, *30*, 538–549. [[CrossRef](#)]
10. Yu, Z.; Xu, H.; Liu, D.; Li, H.; Shi, Y.; Dai, D. Subwavelength-Structure-Assisted Ultracompact Polarization-Handling Components on Silicon. *J. Light. Technol.* **2022**, *40*, 1784–1801. [[CrossRef](#)]
11. Liu, C.; Qiu, J.; Tian, Y.; Guo, H.; Hong, X.; Wu, J. Performance Enhancement of a Broadband Polarization Rotator by using Modified Mode Converters. In *Asia Communications and Photonics Conference; Optical Society of America: Washington, DC, USA, 2018*; p. Su2A–171.
12. Xu, H.; Shi, Y. Subwavelength-grating-assisted silicon polarization rotator covering all optical communication bands. *Opt. Express* **2019**, *27*, 5588–5597. [[CrossRef](#)]
13. Lebbe, N.; Glière, A.; Hassan, K. High-efficiency and broadband photonic polarization rotator based on multilevel shape optimization. *Opt. Lett.* **2019**, *44*, 1960–1963. [[CrossRef](#)]
14. Gallacher, K.; Griffin, P.F.; Riis, E.; Sorel, M.; Paul, D.J. Silicon nitride waveguide polarization rotator and polarization beam splitter for chip-scale atomic systems. *APL Photonics* **2022**, *7*, 046101. [[CrossRef](#)]
15. Yan, X.; Chen, J.; Dai, D.; Shi, Y. Polarization multiplexing silicon-photonic optical phased array for 2D wide-angle optical beam steering. *IEEE Photonics J.* **2021**, *13*, 1–6. [[CrossRef](#)]
16. Dong, P.; Chen, Y.K.; Duan, G.H.; Neilson, D.T. Silicon photonic devices and integrated circuits. *Nanophotonics* **2014**, *3*, 215–228. [[CrossRef](#)]
17. Ma, M.; Park, A.H.; Wang, Y.; Shoman, H.; Zhang, F.; Jaeger, N.A.; Chrostowski, L. Sub-wavelength grating-assisted polarization splitter-rotators for silicon-on-insulator platforms. *Opt. Express* **2019**, *27*, 17581–17591. [[CrossRef](#)]
18. Zhang, Y.; Zhu, Q.; He, Y.; Su, Y. Silicon polarization splitter and rotator with tolerance to width variations using a nonlinearly-tapered and partially-etched directional coupler. In *Optical Fiber Communication Conference; Optical Society of America: Washington, DC, USA, 2019*; p. W1E.4.
19. Xie, C.; Zou, X.; Zou, F.; Zhang, Y. High-performance ultra-compact polarization splitter-rotators based on dual-etching and tapered asymmetrical directional coupler. *Chin. Opt. Lett.* **2021**, *19*, 121301. [[CrossRef](#)]
20. Sacher, W.D.; Barwicz, T.; Taylor, B.J.; Poon, J.K. Polarization rotator-splitters in standard active silicon photonics platforms. *Opt. Express* **2014**, *22*, 3777–3786. [[CrossRef](#)]
21. Chen, X.; Qiu, C.; Sheng, Z.; Wu, A.; Huang, H.; Zhao, Y.; Li, W.; Wang, X.; Zou, S.; Gan, F.; et al. Design of an ultra-broadband and fabrication-tolerant silicon polarization rotator splitter with SiO₂ top cladding. *Chin. Opt. Lett.* **2016**, *14*, 081301–81305. [[CrossRef](#)]
22. Zhao, Y.; Qiu, C.; Wu, A.; Huang, H.; Li, J.; Sheng, Z.; Li, W.; Wang, X.; Gan, F. Broadband polarization splitter-rotator and the application in WDM receiver. *IEEE Photonics J.* **2018**, *11*, 1–10. [[CrossRef](#)]
23. El-Fiky, E.; Wang, Y.; Bernal, S.; Gamache, C.; Panorel, E.; Kumar, A.; Samani, A.; Jacques, M.; Koh, P.c.; Plant, D.V. High extinction ratio and broadband O-band polarization splitter and rotator on silicon-on-insulator. In *Proceedings of the 2019 Optical Fiber Communications Conference and Exhibition (OFC), San Diego, CA, USA, 3–7 March 2019*; pp. 1–3.
24. Chen, Z.; Yang, J.; Wong, W.H.; Pun, E.Y.B.; Wang, C. Broadband adiabatic polarization rotator-splitter based on a lithium niobate on insulator platform. *Photonics Res.* **2021**, *9*, 2319–2324. [[CrossRef](#)]
25. Sun, C.; Yu, Y.; Chen, G.; Zhang, X. A low crosstalk and broadband polarization rotator and splitter based on adiabatic couplers. *IEEE Photonics Technol. Lett.* **2016**, *28*, 2253–2256. [[CrossRef](#)]
26. Rostamian, A.; Guo, J.; Chakravarty, S.; Yan, H.; Chung, C.J.; Heidari, E.; Chen, R.T. Grating-coupled silicon-on-sapphire polarization rotator operating at mid-infrared wavelengths. *IEEE Photonics Technol. Lett.* **2019**, *31*, 401–404. [[CrossRef](#)]
27. Chen, D.; Liu, M.; Zhang, Y.; Wang, L.; Hu, X.; Feng, P.; Xiao, X.; Yu, S. C+ L band polarization rotator-splitter based on a compact S-bend waveguide mode demultiplexer. *Opt. Express* **2021**, *29*, 10949–10957. [[CrossRef](#)]
28. Dai, D.; Wu, H. Realization of a compact polarization splitter-rotator on silicon. *Opt. Lett.* **2016**, *41*, 2346–2349. [[CrossRef](#)]
29. Guo, D.; Chu, T. Broadband and low-crosstalk polarization splitter-rotator with optimized tapers. *OSA Contin.* **2018**, *1*, 841–850. [[CrossRef](#)]
30. Available online: <http://www.hopho.com.cn/khdzfw/31.html> (accessed on 6 October 2022).
31. Dai, D.; Tang, Y.; Bowers, J.E. Mode conversion in tapered submicron silicon ridge optical waveguides. *Opt. Express* **2012**, *20*, 13425–13439. [[CrossRef](#)]